Near-Infrared Lasing in Four-Zigzag Edged Nanographenes by 1D versus 2D Electronic π-Conjugation

Rafael Muñoz-Mármol, Fernando Gordillo, Víctor Bonal, José M. Villalvilla, Pedro G. Boj, José A. Quintana, Aaron M. Ross, Giuseppe M. Paternò, Francesco Scotognella, Guglielmo Lanzani,* Amel Derradji, Juan C. Sancho-García, Yanwei Gu, Jishan Wu,* Juan Casado,* and María A. Díaz-García*

The search of compounds emitting in the near-infrared (NIR) has been accelerated owing to their use in biomedical and telecommunications applications. In this regard, nanographenes (NGs) are attractive materials adequate for integration with other technologies, which have recently demonstrated amplified spontaneous emission (ASE) and lasing across the visible spectrum. Here, the optical and ASE properties of four-zigzag edged NGs of the [*m,n*]*peri*-acenoacene family are reported, whose size is increased through conjugation extension by varying *n* (from 3 to 5) while keeping *m* = 2. Results show that such 1D conjugation extension method is more efficient in terms of shifting the photoluminescence (PL) to the infrared (PL at 710 nm in the larger compound, PP-Ar) than through 2D conjugation extension as in previously reported NGs (PL at 676 nm with the largest compound FZ3, with *n* = 3 and *m* = 4). Additionally, PP-Ar shows dual-ASE (at 726 and 787 nm), whose origin is elucidated through Raman and transient absorption spectroscopies. These compounds' potential for red and NIR lasing is demonstrated through the fabrication of distributed feedback lasers with top-layer resonators. This study paves the way towards the development of stable low-cost all-plastic NIR lasers.

1. Introduction

Conjugated organic materials have been extensively investigated, proving to be particularly suitable for a variety of optoelectronic applications, for example, solar cells, field-effect transistors, and light-emitting diodes, among others. In the last two decades, a considerable part of this effort has been devoted to organic active materials for lasing,[1–3] with a growing interest in materials operating in the near-infrared (NIR) region[4] fueled by the development of biomedical[5] and telecommunication applications.[6] Besides, organic photoluminescent materials present rather large light–matter interaction,[7] and can be integrated with other technologies via cost-effective solution-based processing techniques.[8] For this purpose, bottom-up fabrication approaches via organic chemistry provide smart design and control of the optoelectronic properties with outstanding

R. Muñoz-Mármol, V. Bonal, J. M. Villalvilla, M. A. Díaz-García
Departamento de Física Aplicada and Instituto Universitario de Materiales de Alicante
Universidad de Alicante
Alicante 03080, Spain
E-mail: maria.diaz@ua.es

F. Gordillo, J. Casado
Department of Physical Chemistry
University of Málaga
Andalucía Tech., Campus de Teatinos s/n, Malaga 29071, Spain
E-mail: casado@uma.es

P. G. Boj, J. A. Quintana
Departamento de Óptica
Farmacología y Anatomía and Instituto Universitario de Materiales de Alicante
Universidad de Alicante
Alicante 03080, Spain

A. M. Ross, F. Scotognella, G. Lanzani
Physics Department
Politecnico di Milano
Piazza L. da Vinci 32, Milano 20133, Italy
E-mail: guglielmo.lanzani@iit.it

G. M. Paternò, F. Scotognella, G. Lanzani
Center for Nano Science and Technology
Istituto Italiano di Tecnologia
Via G. Pascoli 70/3, Milano 20133, Italy

A. Derradji, J. C. Sancho-García
Departamento de Química Física and Instituto Universitario de Materiales de Alicante
Universidad de Alicante
Alicante 03080, Spain

Y. Gu, J. Wu
Department of Chemistry
National University of Singapore
3 Science Drive 3, Singapore 117543, Singapore
E-mail: chmwuj@nus.edu.sg

precision and reproducibility.[9] However, organic materials operating in the NIR suffer from the following drawbacks: i) fast non-radiative decay following the energy gap law,[10,11] ii) concentration quenching mechanisms,[2] and iii) excited-state absorption (ESA) promoting charge-separated states, triplets, and other photoproducts[12,13] which ultimately hinder their laser activity.

Over the last decade, graphene has been proposed as a promising material for optoelectronic[14] and spintronic applications.[15] Some initials attempts for opening its vanishing electronic gap[16–18] demonstrated to be insufficient for lasing applications.[19,20] However, shaping graphene into nanostructures (nanographenes, NGs) proved suitable for such applications.[21,22] This strategy relies on the quantum confinement of the electronic wave function to open a finite electronic band gap, which depends on the NG size and the type of edge in their chemical structure (i.e., zigzag or armchair).[23] This enables the tailoring of the NG optoelectronic properties through bottom-up fabrication techniques developed by organic chemistry.[9] For instance, amplified spontaneous emission (ASE) was reported for the first time in NGs combining both armchair and zigzag edges[21] and soon after in four-zigzag (FZ) edged NGs,[22] however it was precluded in cove-edged NGs.[24] Additionally, the effect of adding substituents in several positions of the NG, aiming to increase their solubility and/or to protect them against photoreaction, has been studied in compounds with both, armchair and zigzag edges.[25] Particularly remarkable was the excellent ASE and laser performance (low threshold and large photostability) of a series of three FZ edged NGs of increasing size, denoted as FZ1, FZ2, and FZ3, whose emissions covered a broad range of the visible spectrum and up to the vicinity of the NIR region. These FZ NGs belong to the [n,m]$peri$-acenoacene family, in which a number m of [n]acenes are fused into a rhombic nanoflake, as shown in **Figure 1**. In particular, the FZ compounds have the same n ($n = 3$) and increasing m (2, 3, and 4, for FZ1, FZ2, and FZ3, respectively).

Noticeably, a change from m to $m + 1$ implies the incorporation of 8 π-electrons with the subsequent increase of the conjugation extension (in 2D), which implies a shift in the photoluminescence (PL) emission peaks (from 456 nm, in FZ1; to 547 nm, in FZ2; and to 676 nm, in FZ3) and consequently in the ASE wavelengths.[21] Another interesting result recently reported for the larger compound of this series (FZ3) has been the observation of dual-ASE, that is, simultaneous ASE at two different wavelengths (685 and 739 nm), which was exploited to fabricate distributed feedback (DFB) lasers with emissions at either one or two different wavelengths.[26] Photophysical studies performed with this compound demonstrated the existence of losses in the NIR region, not observed in smaller FZs, which seemed to be involved in the observation of dual-ASE. However, the origin of such losses could not be clearly elucidated.

Contrarily to the expansion of FZ1 towards square-like 2D molecules, here, we explore the effect on the optical, photophysical, and laser properties of FZ edged NGs of increasing conjugation length in 1D direction, that is, from FZ1, we examine the properties of a series of [n,m]$peri$-acenoacenes with the same $m = 2$ and increasing n (3, 4, and 5), denoted as AA-Ar (same as FZ1), TT-Ar, and PP-Ar (see Figure 1), dispersed in polystyrene (PS) films. Results are compared to those of previously investigated FZ NGs, in which the conjugation extension was done in two directions (same $n = 3$) and varying m (2, 3, and 4, for FZ1, FZ2, and FZ3, respectively). The most remarkable result is that in the series investigated here, the red-shift of the PL spectra upon the increase of the compound size, achieved by increasing n, is much larger (from 456 nm, in AA-Ar; to 710 nm, in PP-Ar), than that obtained in the FZ series through the increase of m (from 456 nm in FZ1 to 676 nm, in FZ3). This is particularly significant considering that an increment from n to $n + 1$ in the materials investigated here implies an increment of 6 π-electrons, smaller than the 8 π-electrons increase obtained in the previously reported FZ series upon the increment from m to
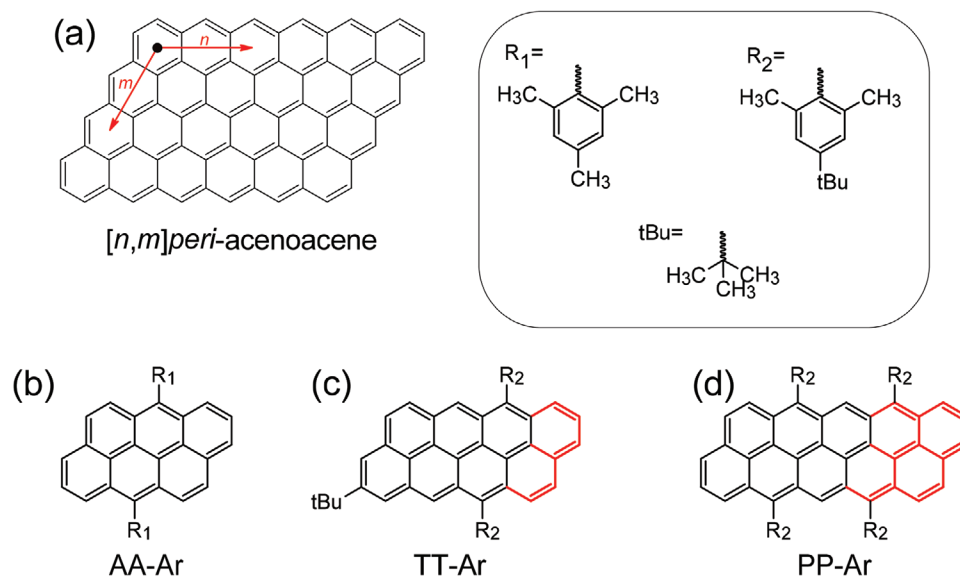
Figure 1. NGs chemical structures. a) Generic n by m four-zigzag edged NG with rhombic shape, termed [n,m]$peri$-acenoacene. b–d) Chemical structures of NGs AA-Ar, TT-Ar, and PP-Ar, respectively, [3,2]$peri$-acenoacene, [4,2]$peri$-acenoacene, and [5,2]$peri$-acenoacene. In red, the incremental part of the core respect to AA-Ar.
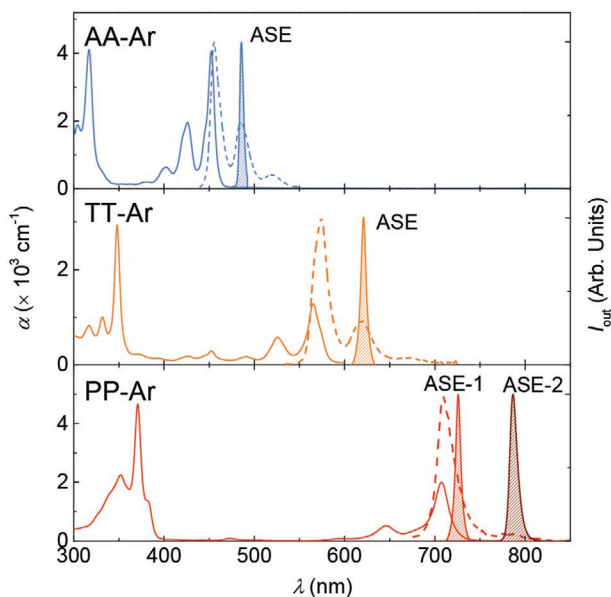
Figure 2. Optical properties of investigated NGs. Absorption coefficient (α; solid lines, left axis), PL (dashed lines, right axis) and ASE (shaded area, right axis) spectra at room temperature of PS films doped with 1 wt% of AA-Ar (top panel, blue), TT-Ar (middle panel, orange) and PP-Ar (bottom panel, red).

$m + 1$. An important consequence of the large PL shifts obtained in the longest 1D *peri*-acenoacene, PP-Ar, is that its ASE lies fully in the NIR region. Besides, this compound shows dual-ASE at 726 and 787 nm. Cryogenic steady-state absorption and emission, Raman and ultrafast transient absorption (TA) spectroscopies are jointly used to assign the vibronic transitions of the PL spectra to specific molecular vibrations, at some of which ASE occurs, in some cases in dual-modality. As a culmination, we manufacture DFB lasers to demonstrate the suitability of this compound for lasing applications in the NIR.

2. Results and Discussion

The analyzed samples consist of PS thin films with either TT-Ar or PP-Ar dispersed at 1 wt%. Such concentration was found to optimize the ASE and lasing properties in similar systems.[21,22] These NG-doped films were prepared by

spin-coating a toluene solution of the precursors on top of a quartz substrate. Film thickness (h_f) was adjusted to ensure that only fundamental transversal modes (electric and magnetic, TE_0 and TM_0 respectively) are supported in the resulting waveguide, and present a high confinement factor ($\Gamma \approx 90\%$). Under such conditions, waveguide losses are minimized and the ASE performance-optimized.[27,28] Results for the previously reported FZ1 (hereinafter called AA-Ar, for coherence in nomenclature) will be included in figures and discussions to help in the comparisons.[22]
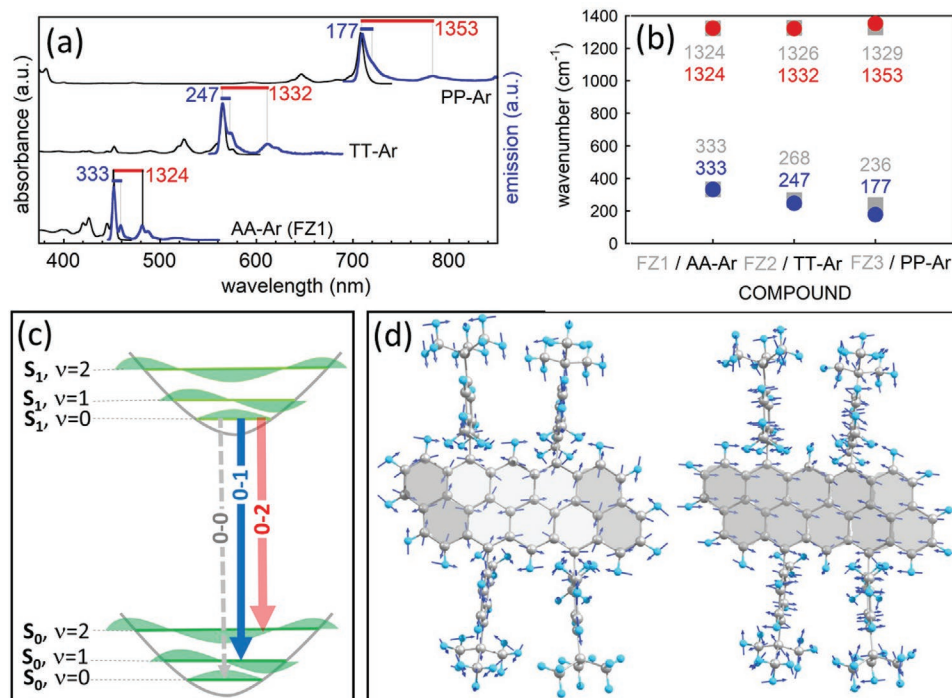
2.1. NGs Optical Properties

The absorption and PL spectra of the NG series investigated cover a large part of the visible spectrum, entering into the NIR (see **Figure 2** and **Table 1**). Noticeably, the spectra of TT-Ar and PP-Ar are significantly red-shifted, with respect to those of their FZ2 and FZ3 counterparts (by 20 and 39 nm, in the corresponding absorption spectra, and by 27 and 34 nm in their PL spectra, respectively). Particularly interesting are the properties of PP-Ar, whose PL spectrum lies fully in the NIR region, in contrast to FZ3, whose edge spectrum presented just 10% beyond 700 nm.[22] Remarkably, high PL quantum yield values are found for TT-Ar and PP-Ar, reaching up to 72% (see Table 1), which are similar values to those reported for the previous FZ series of NGs. The singlet excited-state (absorption) energies for the investigated NGs, obtained via multi-configurational NEVPT2/def2-SVP calculations (see Figure S1, Supporting Information), reasonably agree with the experimental results from Table 1: 407, 544, and 711 nm, for AA-Ar, TT-Ar, and PP-Ar, respectively, indicating a negligible matrix effect and corroborating the progressive red-shift upon increasing the fully and rigid conjugated backbone of these compounds, as expected.

In order to get insights on the origin of the different transitions in these spectra, we performed absorption and PL measurements at low temperature, LT (N_2 liquid temperature, 80 K) in methyl tetrahydrofuran (THF) solution as well as Raman characterization, that is, with resonant and pre-resonant conditions in the solid-state. **Figure 3**a displays the LT absorption/PL spectra of AA-Ar, TT-Ar, and PP-Ar. The LT-PL spectra allow to distinguish two main vibrational progressions, the strong 0–1 and a weak 0–2 one with spacings of 333/1324 cm^{-1} in AA-Ar, 247/1332 cm^{-1} in TT-Ar, and 177/1352 cm^{-1} in PP-Ar measured from the maxima of the 0-0 bands (fundamental transitions)

Table 1. Optical parameters of investigated NGs, dispersed in PS films at 1 wt%.

Nanographene	λ_{ABS} [nm][a]	λ_{PL} [nm][b]	PLQY [%][c]	λ_{pump} [nm][d]	λ_{ASE} [nm][e]	FWHM [nm][f]	$E_{th\text{-}ASE}$ [mJ cm^{-2}][g]	$\tau_{1/2}$ (E_{pump}) [×10^5 pp (mJ cm^{-2})][h]
AA-Ar	402/426/<u>452</u>	<u>455</u>/485/519	82	452	486	4	0.045	0.2 (0.20) *
TT-Ar	491/526/<u>565</u>	<u>574</u>/619	72	565	621	7	0.10	5 (0.40)
PP-Ar	646/<u>707</u>	<u>710</u>/785		646	726	6	60	0.4 (80)
					787	9	1.5	10 (6.0)

[a]Wavelengths of main absorption lines, the underlined value corresponds to the most intense peak; [b]Wavelengths of main photoluminescence lines, the underlined value corresponds to the more intense peak; [c]Photoluminescence quantum yield (error ≈ 10%); [d]Pump wavelength; [e]Amplified spontaneous emission wavelength (error ±0.7 nm); [f]Amplified spontaneous emission linewidth, defined as full width at half maximum well above the threshold (error ±1.3 nm); [g]Amplified spontaneous emission threshold expressed as energy density (error ≈ 10%); [h]Photostability half-life parameter expressed in pump pulses (error ≈ 20%). The experimental pump fluence is indicated in brackets. *) Value extracted from ref. [22].

**ADVANCED
SCIENCE NEWS**
www.advancedsciencenews.com

**ADVANCED
FUNCTIONAL
MATERIALS**
www.afm-journal.de

Figure 3. Optical and vibrational Raman properties of investigated NGs; a) Low temperature (80 K) absorption (black lines) and PL (blue lines) of the three NGs showing the low (0-1, blue sticks) and high (0-2, red sticks) wavenumber progressions. b) Variation of the wavenumber of the two progressions in the two series of *peri*-acenoacenes. c) Qualitative vibronic transitions to account for the vibronic progressions. d) Normal modes associated with the Raman modes of the two progressions in PP-Ar.

in the absorption and PL spectra (each spectrum is thus composed of two vibronic bands with two components each). The two progressions disclose different chain length dependence as the high wavenumber one is rather constant in the three NGs, whereas the case of the low wavenumber moves down from AA-Ar to PP-Ar. This might alert us of different electron-vibration couplings based on different length-dependent behaviors. On the homolog series of FZ1-3 *peri*-acenoacenes, we observed similar progressions whose wavenumbers are represented in Figure 3b in comparison with those of the compounds under study.[22] We see, again, that the high wavenumber progression slightly depends on the molecular size while that at low wavenumbers displays a greater size dependence. Comparing both series, the total variation of the low wavenumber progression in the three compounds is larger in the AA-Ar/TT-Ar/PP-Ar series. These data reveal, as discussed below, the connections with the different electronic delocalization in the two series, originated by the different ratio between edge and bulk π–domains.

The Raman spectra (Figure S2, Supporting Information) taken in resonance with the dominant electronic absorption bands of the three NGs show weak and strong bands (in parenthesis the strongest band) at 342/1350(1321) cm^{-1} in AA-Ar, 222/1352(1376) cm^{-1} in TT-Ar and (-)/1340(1322) cm^{-1} in PP-Ar, which matches well with the evolution among the three NGs of the vibrational progression wavenumbers from the LT-PL spectra. With quantum-chemical calculations, we have reproduced the resonant Raman spectrum of PP-Ar (see Figure S3, Supporting Information) and found the vibrational normal

modes associated with the above-mentioned experimental Raman bands and therefore representative of the vibronic modes in the optical spectra. The vibrational eigenvectors of these two modes are in Figure 3c, which can be described as: i) the higher wavenumber mode (i.e., theoretically calculated at 1381 cm^{-1} in PP-Ar in Figure S3, Supporting Information) is an in-plane CC stretching vibration which spreads mostly on the external naphthalene-like groups of PP-Ar (grey dashed rings in Figure 3d); while ii) the lower wavenumber band (i.e., theoretically calculated at 248 cm^{-1} in PP-Ar in Figure S3, Supporting Information) can be defined as an in-plane CCC deformation, or bending, vibration spreading over the whole molecular PP-Ar entity. This is interesting as it can justify the observed trends of the vibronic progressions, given that the progression associated with the bending mode is more sensitive to the enlargement of the molecular size (it spreads over the whole *peri*-acenoacene). On the other hand, the progression associated with the CC stretching mode is less dependent on the size as it mostly involves the terminal parts that are "invariant" upon enlarging the core from AA-Ar to PP-Ar.

The electronic structure of graphene nanoribbons is described in terms of the so-called bulk and edge states attending to the localization of the wavefunctions either in the peripheral or in the innermost parts.[29] In finite or discrete molecular NGs, with the increase of the molecular size (such as in the AA-Ar→FZ3 and in AA-Ar→PP-Ar), the bulky versus edge electronic phases will progressively differentiate (becoming fully independent phases in large NGs), an effect that could also be the case of the topological distribution of

**ADVANCED
SCIENCE NEWS**

www.advancedsciencenews.com

**ADVANCED
FUNCTIONAL
MATERIALS**

www.afm-journal.de

the overall oscillator strength in the optical excitations such as delineated by the vibronic progressions under discussion. In other words, we could have an $S_0 \rightarrow S_1/S_1 \rightarrow S_0$ transition with oscillator strengths distributed along the long and short zigzag edges or axis. In Figure 3c, we show a qualitative diagram of the vibronic eigenfunctions of the ground (S_0) and first (S_1) excited states (those relevant in the optical properties of the studied NGs). These two S_0/S_1 states lay one on the top of the other, or nested states, owing to the small Stokes shifts in the absorption/PL spectra. As a result, the 0-0 component is the strongest transition since it carries out maximal overlap of the ($S_1, v = 0$) and ($S_0, v = 0$) vibronic wavefunctions. This is followed by the 0–1 and 0–2 vibronic bands which acquire significant amounts of oscillator strengths since the important overlap available for the ($S_1, v = 0$)/($S_0, v = 1$) and ($S_1, v = 0$)/($S_0, v = 2$) excitations. Nonetheless, for transitions involving higher vibrational quantum numbers, overlaps decrease and the intensities of the corresponding vibronic bands become concomitantly lower.

2.2. ASE Properties

In order to exploit the properties of the investigated NGs, prepared as thin films, for laser applications, their ASE properties have been first evaluated. This phenomenon can be recognized as a narrowing of the PL spectrum accompanied by a sudden increase of the output intensity (I_{out}) at a given pump energy density (E_{pump}) value, the so-called ASE threshold (E_{th-ASE}). The NGs investigated here all show ASE (see spectra in Figure 2 and most relevant parameters in Table 1, i.e, emission wavelengths, thresholds, and operational lifetime).

An important feature is the significant red-shifted ASE observed in TT-Ar and PP-Ar, in comparison to that reported in FZ2 and FZ3. Particularly, TT-Ar shows ASE at 621 nm, which is 30 nm above the ASE reported for FZ2 (591 nm).[22] Besides, PP-Ar shows dual-ASE, that is, simultaneous ASE at two different wavelengths, both in the NIR (at 726 and 787 nm). These values are more than 40 nm red-shifted with respect to those reported for FZ3, which displayed dual-ASE at 685 and 739 nm.[26] These results indicate that the strategy of increasing n followed in the series reported here (AA-Ar, TT-Ar, and PP-Ar) to obtain emissions at larger wavelengths is more NIR emitter efficient in terms of conjugation than that of increasing m (followed in the previous series AA-Ar, FZ2, FZ3), as a larger red-shift is observed with a lower increase in π-electrons. In other words, this means that electronic delocalization is more efficient in the compounds with larger but highly asymmetrical edges (pentacene-like versus tetracene-like, in PP-Ar versus FZ3, respectively) rather than in systems with larger total number of benzene rings (i.e.; 10 in PP-Ar versus 12 π-electrons in FZ3). This is corroborated by calculating the averaged value of the index known as HOMA (Harmonic Oscillator Model or Aromaticity) from the PBEh-3c optimized structures of both PP-Ar (TT-Ar) and FZ3 (FZ2) compounds, all along the larger edge of the compounds: 0.72 (0.73) and 0.56 (0.71) respectively, thus pointing to a clear (and more marked) electronic delocalization on the edge for PP-Ar compared to FZ3.

ASE in TT-Ar and PP-Ar seemingly emerges from light amplification of the 0–2 vibronic component, with reabsorption acting detrimentally over the strongest 0-0 and 0–1 vibronic components. On the other hand, in PP-Ar, besides the typical ASE peak at the 0–2 vibronic site, an additional ASE peak is seen at the wavelength of the 0–1 vibronic component. The underlying mechanisms behind the ASE performance of these compounds will be discussed in next section in the frame of TA spectroscopy experiments performed in the films.

Regarding the ASE thresholds of the investigated NG-based films, they were determined from plots of I_{out} and linewidth (defined as the full width at half maximum, FWHM) versus E_{pump} (see illustrative example in Figure S4, Supporting Information). Among the different ways reported in literature for determining E_{th-ASE},[30] we have chosen the one based on the emission linewidth (FWHM) evolution with the pump energy density to enable comparisons to previously reported values with similar compounds, for which this method was used.[22,26] Thus, E_{th-ASE} corresponds to the pump energy density at which the FWHM reaches the average value between the ones observed at low and high excitation density, which approximately coincides with that at which a drastic slope change in I_{out} is seen. The obtained results are listed in Table 1. Most remarkable is the performance of PP-Ar, which displays thresholds of 60 and 1.5 mJ cm^{-2} for the ASE-1 and ASE-2 peaks, respectively, comparable to those reported for FZ3, whilst now the emission occurs at significantly longer wavelengths. These ASE thresholds are higher than those previously reported for other organic compounds emitting in the NIR, as it is the case of certain organic dyes dispersed in polymeric matrixes ($E_{th-ASE} \approx 100$ µJ cm^{-2}), thermally activated delayed fluorescence dyes dispersed in molecular media (≈ 10 µJ cm^{-2}), or organic single crystals (≈ 1–1000 µJ cm^{-2}), see further details in Table S1, Supporting Information.[3,4] The reason for the larger thresholds is discussed at the end of the TA section.

With regards to the ASE operational durability in ambient conditions of the investigated NGs, it is excellent, as discussed below, in accordance with results obtained with other NGs, such as the FZ1-3. This property is analyzed by observing the evolution over the time (or the number of pump pulses) of the ASE peak intensity under uninterrupted pump (see illustrative example in Figure S4f, Supporting Information) and quantified by the so-called ASE half-life parameter ($\tau_{1/2}$), defined as the time (number of pump pulses) needed for the output intensity to reach half of its initial value (see results in Table 1). Noticeably, for the ASE-2 peak ($\lambda_{ASE-2} = 787$ nm) of PP-Ar, a value as large as $\tau_{1/2} \approx 10^6$ pump pulses (under a pump intensity four times above its threshold) was measured. Under similar pumping conditions, a value two times smaller was obtained for TT-Ar. On the other hand, the emission at the ASE-1 peak of PP-Ar showed a shorter lifetime ($\tau_{1/2} = 3.5 \times 10^4$ pump pulses), which is attributed to its larger threshold, which required a larger pump intensity to be above threshold (see details in Table 1). Such outstanding photostability performance is comparable to that of previously reported NGs.[21,22] Particularly, PP-Ar is among the most photostable organic compounds emitting in the NIR, despite the fact that it needs to be pumped at a higher energy density due to its larger threshold (see Table S1, Supporting Information).

2105073 (5 of 10)
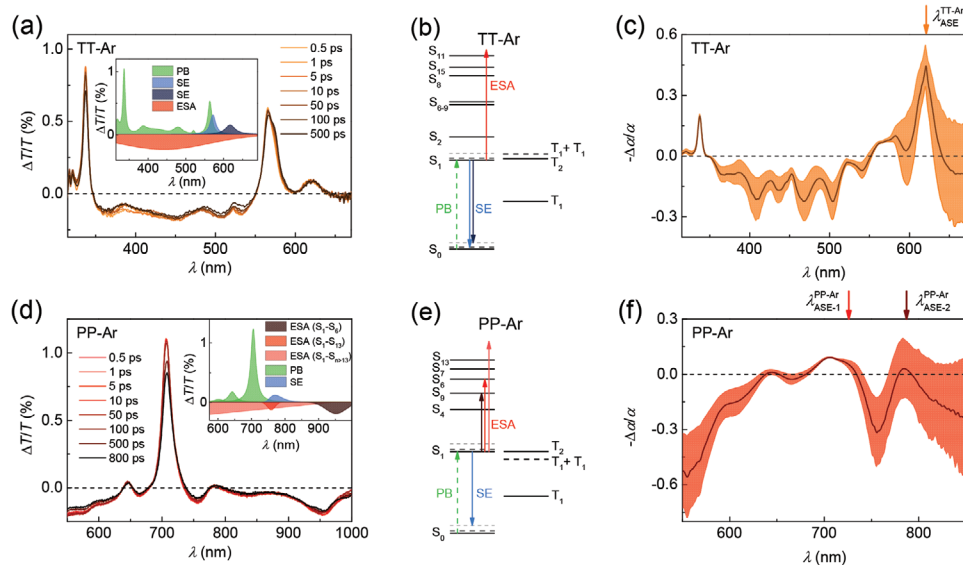
Figure 4. TA spectra and excited-state energy levels. a,d) TA spectra for TT-Ar and PP-Ar, respectively, dispersed in PS films (1 wt%). The collection parameters are indicated in Table S2, Supporting Information. Insets show the spectrum deconvolution. b,e) excited-state energy levels of TT-Ar and PP-Ar, respectively, obtained via NEVPT2 calculations. The principal deconvoluted components of the TA spectrum are indicated with arrows. c,f) pump-induced absorption coefficient normalized to steady-state absorption coefficient, $-\Delta\alpha/\alpha$, for PS films doped with TT-Ar and PP-Ar, respectively. The shadows correspond with the estimated error and the arrows mark the ASE wavelengths.

2.3. NGs TA

Subsequently, we characterized the TA spectra of TT-Ar and PP-Ar (**Figure 4**) to understand the underlying photophysical processes cohabitating with ASE upon excitation. Two differential features are present in the TA spectra of PP-Ar with respect to that of TT-Ar, which consist of two negative bands at wavelengths longer than that of the fundamental electronic transition ($S_0 \rightarrow S_1$). As discussed in detail below, such differential features appear to be responsible for the observation of dual-ASE in this compound. Noticeably, in a recent study with FZ3, dual ASE was also reported and related to the observation of a structureless negative band in the TA spectrum.[26] However, the interpretation of the physical underlying mechanisms remained elusive

The TA spectra of TT-Ar and PP-Ar present several features associated with different phenomena, which can be deconvoluted by fitting a global function (inset Figure 4a,d). Common for both NGs are the main positive peak and their blue-shifted positive peak attributed to photobleaching (PB) from the ground state absorption. Actually, a differential feature appears in the spectrum of TT-Ar, whose main transition is composed of two peaks, one at 565 nm and the other at 573 nm, attributed to PB and stimulated emission (SE), respectively. Another common characteristic of both NGs is the presence of SE, revealed by the positive peaks observed at the red side of the main transition, coinciding spectrally with their 0–2 vibronic transition. Furthermore, these NGs present a certainly broad negative band superimposed on all of the PB features, which is attributed to ESA from higher energy electronic states. On the other hand, in PP-Ar (but not in TT-Ar), additional negative bands appear at longer wavelengths than that of the main electronic transition ($S_0 \rightarrow S_1$), which partially cancels its SE band.

These two negative peaks at around 761 and 950 nm are attributed to ESA to upper energy lying electronic states. Specifically, those bands correspond with the transitions $S_1 \rightarrow S_7$ and $S_1 \rightarrow S_9$, respectively, as supported by the NEVPT2 theoretical calculations (Figure 4b,e).

In the case of FZ3, a feature-less negative band was observed at wavelengths <666 nm, whose uncertain origin was speculatively attributed to a charge-separated state through comparisons with acenes.[26] According to results obtained with PP-Ar, it is possible that ESA might also be present here. In fact, the existence of a charge-separated state in FZ3, or even in PP-Ar cannot be discarded, as these NGs present a certain diradicaloid character.[31] This is also corroborated here by means of FT-DFT calculations, which predict some fractional orbital occupation of the orbitals close to the Fermi level. Diradicaloid molecules have been proposed as good candidates hosting singlet exciton fission processes, which could be mediated by CT states before yielding the diradicaloid stabilized triplets.[32] Note that the outcome of those FT-DFT calculations predicts a higher diradicaloid character for PP-Ar than for TT-Ar, and for TT-Ar than for AA-Ar, in agreement with extended zigzag edges. Quantitatively speaking, we define the (poly)radicaloid character of any compound by the index (y_0, y_1) arising from the fractional occupation (y_i) of the LUMO and LUMO+1 orbitals, respectively.[33] A pure closed-shell, diradical, or tetraradical system will thus exhibit ideal (y_0, y_1) values of (0,0), (1,0), and (1,1), respectively, with more moderate values meaning diradicaloid or tetraradicaloid character. In this case, we obtain (0.19,0.02), (0.35,0.04), and (0.52,0.08) values for AA-Ar, TT-Ar, and PP-Ar, respectively, which indicates a progressive increase of their radicaloid character with system size. Such mechanism would result in PL quenching, hindering light amplification. We also analyzed the electronic absorption

spectra of the radical anions and cations in methyl THF solutions for TT-Ar and PP-Ar, which are supposed to represent the structure of the charge-separated transient species that would be generated upon photoinduced electron transfer, as shown in Figure S5, Supporting Information. We observe that the radical species of PP-Ar absorb intensely in the range over 1200 nm, while they also show medium absorbance bands below 600 nm, leaving free of absorption the relevant range for ASE between 700–800 nm. In the case of TT-Ar, the low energy bands of the electronic absorption spectra of the radical species all appear passed 1000 nm, but they show intense absorption between 570 and 630 nm, in coincidence with the SE band. From these data, we see that under the hypothesis of charge-separated states formation, these would interfere more actively in the case of TT-Ar than in PP-Ar. Consequently, for the purpose of explaining the negative features of the TA spectrum implied in the observation of dual ASE, ESA seems to be the dominant mechanism.

The differences observed between the ASE performances of both NGs can be clarified through the analysis of the pump-induced change in the absorption coefficient, relative to the steady-state absorption coefficient ($-\Delta\alpha/\alpha$). This parameter encloses the gain information of the system, where three main regions can be differentiated: 1) negative values, which correspond to pump-induced losses; 2) positive values lower than 1, that correspond to pump-induced gain not enough for overtaking losses; and 3) positive values larger than 1, that correspond with pump-induced gain higher than losses and light amplification. In our case, the values of $-\Delta\alpha/\alpha$ will be always below 1 because the pump intensity was maintained below the amplification threshold (ASE threshold). Figure 4c shows the $-\Delta\alpha/\alpha$ spectrum of TT-Ar-doped films, displaying two positive bands with different intensities that spectrally coincide with the two PL peaks. Thus, the ASE emission of TT-Ar is attributed to the dominant pump-induced gain band that peaks at 621 nm ($\lambda_{ASE} = 621$ nm). Similarly, PP-Ar presents two pump-induced gain bands spectrally coincident with the PL peaks, but this time both present similar intensities, see Figure 4f. This is a direct consequence of the partial cancelation of the SE peak at 775 nm by the negative ESA bands observed in the film TA spectrum. These two pump-induced gain bands of similar value are certainly responsible for the dual-ASE performance of PP-Ar, as both grow up approximately at the same time with the pump energy density (Figure S6, Supporting Information). Then, the ultimate cause for the dual-ASE emission in PP-Ar can be attributed to the presence of the negative ESA band observed in the TA spectrum, which balances both gain bands. Actually, the existence of ESA appears to be the main reason for the larger ASE threshold found in PP-Ar compared to other organic compounds emitting in the NIR, see Table S1, Supporting Information. Currently, novel NGs with electronic states molecularly designed to cope with this issue are under investigation.

2.4. NG-Based DFB Lasers

DFB lasers have been fabricated and properly characterized to ascertain the convenience of these NGs for lasing applications. The device architecture (**Figure 5**a) includes a top-layer polymeric resonator deposited on top of the NG-doped PS film. Such resonator consists of a 1D relief grating engraved by holographic lithography (HL) and subsequent dry etching on a water-soluble dichromated gelatin (DCG) photoresist layer. The implementation of the resonator in a separated layer, located on top of the active film, presents some advantages with respect to other designs.[34] First, the deposition of the DCG layer from water preserves the optical properties of the active film, which is only affected by organic solvents. Second, devices emitting at different wavelengths and maintaining low thresholds for all of them became feasible, by virtue of the HL versatility and uniform active film thickness.

All the devices prepared rely on 1D gratins operating in the second diffraction order ($m = 2$) of the Bragg condition (Equation 1):

$$m\lambda_{Bragg} = 2n_{eff}\Lambda \tag{1}$$

where n_{eff} is the effective refractive index of the waveguide, which depends on h_f and the resonator depth (d; $\approx$90 nm in all devices analyzed) and the refractive indexes of substrate, active film, grating, and cover; and Λ is the grating period. In second-order DFBs, light emission is out-coupled perpendicularly to the device surface by first-order diffraction at a wavelength λ_{DFB} close to λ_{Bragg}. For light propagating in a given waveguide mode (in the designed devices, either TE$_0$ or TM$_0$) and a pure index grating in a separated layer (as the present case), couple mode theory[35] predicts the formation of a photonic stop-band (a dip) centered at λ_{Bragg} and lasing taking place at two wavelengths, one at each edge of the dip. Then, Λ is tailored to provide that λ_{Bragg} approximately matches λ_{ASE}, at which the gain is maximum and the threshold minimum. Even so, in the case of second-order devices, single-mode emission at the peak of longer wavelength is found, which is attributed to the higher radiation losses at shorter wavelengths.[36]

The geometrical and operational parameters for the various DFB devices fabricated are gathered in **Table 2**. For each NG, various devices with different Λ were analyzed to match the lasing action with the gain maximum, taking advantage that λ_{DFB} changes with Λ. The emission spectra of these devices are shown in Figure 5b. The two lasers fabricated with TT-Ar emit between 620 and 628 nm, showing two peaks each. Every peak corresponds to a lasing mode, which can be associated with a certain waveguide mode (either TE$_0$ or TM$_0$) by examining its polarization properties. The peak with polarization parallel to the grating lines is identified with the TE$_0$ mode of the waveguide, while the one polarized perpendicularly to the grating lines is related to the TM$_0$ mode. This association is supported through calculations of λ_{Bragg} (through Equation (1)), using the n_{eff} calculated for each waveguide mode. Notice that the emission polarization is independent of the pump beam polarization.

Most remarkable are the devices fabricated with PP-Ar, because their emission lies fully into the NIR (between 729 and 795 nm). Moreover, the spectral range covered is rather large, thanks to the dual ASE emission, so devices can be designed to emit close to each of the two ASE peaks. So, three devices were fabricated, one design to emit close to the first ASE peak ($\lambda_{ASE-1} = 726$ nm, $\lambda_{DFB} = 728.8$ nm) and two others to emit close
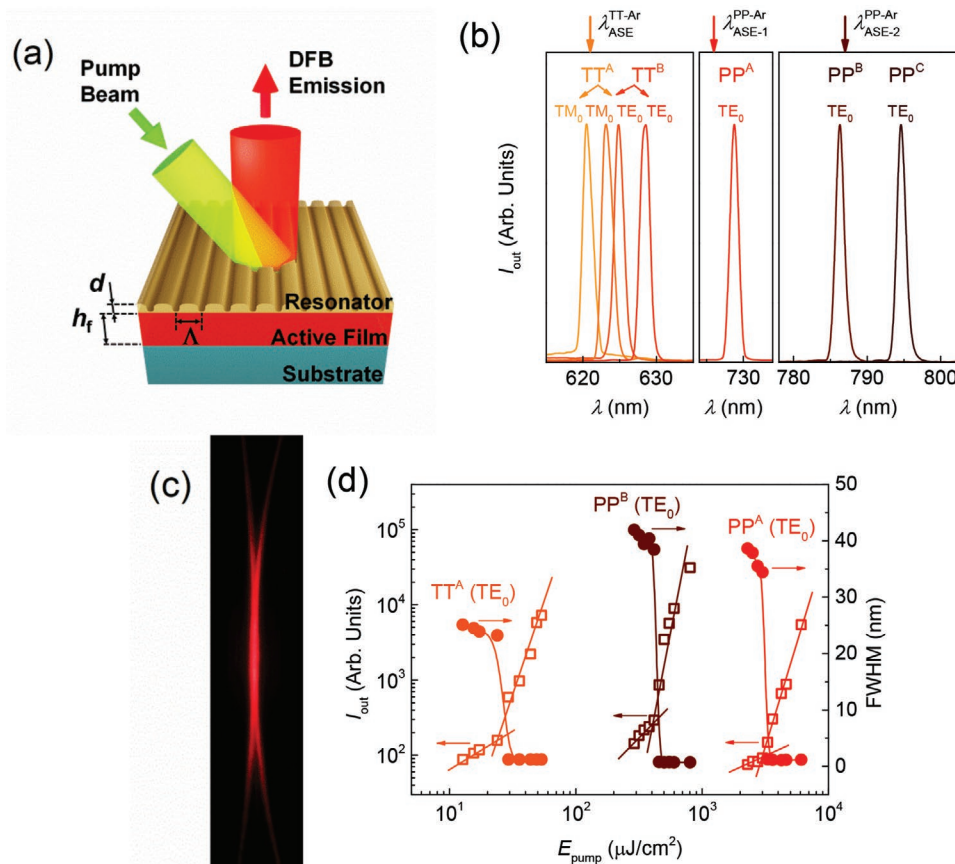
Figure 5. NG-based DFB lasers. a) Design of a DFB laser device based on a relief grating resonator of period Λ and depth d on top of the active film of thickness h_f. b) Spectra of DFB lasers based on NG-doped PS films: the label indicates the NG dispersed in the film and letters are used to discern devices with different geometrical parameters. Each laser emission is composed of either one or two peaks (laser modes), which are associated with the waveguide mode (TE$_0$ or TM$_0$) and whose polarization is parallel or perpendicular to the DFB grating lines, respectively. The top arrows indicate the wavelength of the nearest ASE peak. c) Image of the light emitted by device TT^A. d) Emission output intensity (I_{out}; open squares, left axis) and linewidth, defined as the FWHM (full circles, right axis) as a function of the pump energy density (E_{pump}) for the laser peaks associated with TE$_0$ waveguide mode of devices TT^A, PP^A, and PP^B. Lines are guides to the eye.

Table 2. Laser devices parameters.

Laser device[a]	h_f [nm][b]	Λ [nm][c]	λ_{pump} [nm][d]	λ_{DFB} [nm][e]	$E_{th\text{-}DFB}$ [μJ cm^{-2}][f]
TT^A	520	403.2	565	620.6 (TM$_0$)	47
				624.9 (TE$_0$)	25
TT^B	520	405.5	565	623.0 (TM$_0$)	38
				627.6 (TE$_0$)	34
PP^A	500	471.6	646	728.8 (TE$_0$)	3100
PP^B	500	511.3	646	786.3 (TE$_0$)	430
PP^C	500	517.7	646	794.6 (TE$_0$)	600

[a]The device consists of an active film of polystyrene doped with 1 wt% (error ≈ 0.1%) of nanographene with a top-layer of dichromated gelatin with an engraved relief grating; [b]Film thickness (error ≈ 2%); [c]Grating period (error ≈ 0.5%); [d]Pump wavelength; [e]DFB wavelength (error ±0.7 nm) for each laser peak (laser mode) observed in the emission spectrum. The waveguide mode (TE$_0$ or TM$_0$) to which the laser mode is associated is shown in brackets. The emitted laser light is polarized parallel (for TE$_0$) or perpendicular (TM$_0$) to the DFB grating lines; [f]DFB threshold expressed as energy density (error ≈ 10%).

to the second ASE peak ($\lambda_{ASE\text{-}2}$ = 787 nm; λ_{DFB} = 786.3 and 794.6 nm). All of them show just one emission peak polarized parallel to the grating lines, then associated with the TE$_0$ mode of the waveguide. Thus, these DFBs are to date the NG-based lasers emitting further into the NIR.

Figure 5c shows the beam profile for a DFB laser based on TT-Ar, well above its laser threshold. Here, the light emitted presents the red color identified with the 620–628 nm range, forming the two characteristic arcs associated with DFB laser emission. This laser beam presents a divergence of ≈1.8×10^{-3} rad, in the direction perpendicular to its grating lines.

The DFB threshold values ($E_{th\text{-}DFB}$) have been determined from plots of the spectrum linewidth (FWHM) and of I_{out} as a function of E_{pump}, such as those represented in Figure 5d. At the threshold, the emission spectrum collapses into a narrow peak (FWHM = 1.3 nm, limited by the spectrophotometer resolution). The devices based on TT-Ar perform fairly well in terms of threshold, showing values between 25 and 47 μJ cm^{-2} (5.7–11 kW cm^{-2}), see Table 2. These values are slightly superior to those of state-of-the-art DFB lasers emitting in the same band of the spectrum and based on a perylenediimide derivative

**ADVANCED
SCIENCE NEWS**

www.advancedsciencenews.com

**ADVANCED
FUNCTIONAL
MATERIALS**

www.afm-journal.de

(22 μJ cm^{-2}),[37] a carbon-bridged oligo(p-phenylenevinylene) (7 μJ cm^{-2})[38] and FZ2 (11–18 μJ cm^{-2}).[22] On the other hand, the threshold performance of PP-Ar-based devices depends on whether they are designed to emit close to the first or the second ASE peak. The device emitting close to the first ASE peak shows a threshold of 3100 μJ cm^{-2}, while those emitting at the second ASE peak present significantly lower values (430–600 μJ cm^{-2}). Noticeable, the thresholds of these devices are 3 times lower than those previously reported for FZ3 (with emissions at either 689.5 or 744.5 nm, associated with TE$_0$ modes).[26]

3. Conclusion

We studied the optical and lasing properties of two new FZ-edged NGs of increasing conjugation length, TT-Ar and PP-Ar, displaying ASE at 621 nm and dual-ASE at 726 and 787 nm, respectively. Both NGs belong to the family of *peri*-fused structures, consisting of an *m* number of [*n*]acenes fused into a rhombic nanoflake, [*n,m*]*peri*-acenoacenes. Particularly, TT-Ar and PP-Ar consist of extensions of the previously reported AA-Ar (or FZ1; [3,2]*peri*-acenoacene) generated by increasing *n*, while *m* is fixed (*m* = 2). This conjugation strategy represents an improvement with respect to the previously used to generate the compounds FZ2 and FZ3, that was by increasing *m* while *n* was fixed (*n* = 3), as longer wavelengths are reached with a lower increase of π-electrons. These NGs might present a certain competition between bulk- and edge-like states, with the new conjugation strategy favoring the last. Interestingly, PP-Ar PL spectra are fully placed into the NIR region while for FZ3 was just 10%. Additionally, the origin of the dual-ASE emission was investigated by both Raman and TA spectroscopies. The results evidence that each ASE peak is related to a different vibronic mode. That is the first ASE peak corresponds to an in-plane CCC deformation, or bending, mode (≈200 cm^{-1}), while the second ASE peak is related to an in-plane CC stretching mode (≈1300 cm^{-1}). Although, both modes are present in both NGs, the gain peak associated with the stretching mode is typically larger than that of the bending mode. Thus, ASE emission is observed only from the former. However, ESA to higher-lying states equilibrates both gain bands in PP-Ar, allowing the dual-ASE emission. We also demonstrated the convenience of both NGs for lasing applications with the manufacture of DFB devices, emitting in the surroundings of their ASE peaks. Particularly, a DFB laser based on PP-Ar with emission at 794.6 nm has been prepared, which converts it into the laser-based on NGs operating further in the NIR region.

4. Experimental Section

Synthesis: The NGs TT-Ar and PP-Ar were synthesized by following the multi-step procedures previously reported.[31]

Films and Resonator Preparation: Thin films of PS with 1 wt% of either TT-Ar or PP-Ar dispersed inside were fabricated by spin-coating, using toluene as solvent, over quartz substrates. The film thickness was adjusted by controlling the relative amount of solvent to PS and its value was determined from the interference pattern present in the absorption-free part of the absorption spectrum by an interferometric method.[39]

The DFB resonators were fabricated following a multi-step recipe: 1) A 100 nm thick DCG photoresist layer was deposited over the active film by spin-coating a hot water solution (40 °C, 2.2 wt%); 2) The DCG film was exposed to a 1D light pattern generated by HL with an average exposure of 45 mJ cm^{-2} using an Ar laser (λ = 364 nm) in Lloyds configuration;[40] 3) The DCG layer was desensitized in a cool-water bath (15 °C) and then subjected to a dry etching process with an oxygen plasma provided by a surface treatment machine (Diener Zepto; 10 min). As a result, a relief grating of depth 90 nm and rectangular grating profile with duty cycle 0.75:0.25 was obtained.[34,40,41]

Room-Temperature Absorption and PL of Thin Films: The RT absorption and PL film spectra were measured with a double-beam spectrophotometer (Jasco V-650) and a Horiba Nanolog fluorimeter, respectively. PL quantum yield was characterized with an integrating sphere (Jasco ISF-834) attached to a fluorimeter (Jasco FP-6500).

Computational Calculations: The FT-DFT calculations were done with the TPSS exchange-correlation functional and with the large def2-TZVP basis set to avoid basis set incompleteness issues. For the FT-DFT (also known as FOD) method,[42] the default electronic temperature of 5000 K was fixed. The NEVPT2/def2-SVP calculations[43] were based on a CASSCF(6,6) active space for all the systems, built from MP2 natural orbitals, and demanded a large number of roots (×20) of each multiplicity, singlet, and triplet. The geometries of all the studied compounds were fully optimized by the PBEh-3c method,[44] leading to all-real 3N-6 vibrational frequencies in all cases. All the calculations were done with auxiliary basis sets, tighter-than-default numerical thresholds, and using the 4.0.1.2. release of the ORCA quantum-chemical package.[45]

ASE and Lasing: The characterization of the ASE properties, of active films without resonator, and the laser properties, of films with DFB resonators, were performed under excitation with a built-in optical parametric oscillator pumped with the third harmonic of a pulsed Nd:YAG laser (10 Hz; 355 nm). The pulse width at 565/646 nm was 4.4/4.6 ns. The pump energy density impinging over the samples was varied using neutral density filters. For ASE measurements, the beam was shaped into a stripe (3.5 mm × 0.5 mm) with a cylindrical lens and an adjustable slit and then projected perpendicularly over the sample. The emitted ASE light was collected from the sample edge with an optical fiber coupled to a fiber spectrophotometer (Ocean Optics, USB2000+ UV–VIS) of 1.3 nm resolution. For DFB characterization, the pump beam was focused with a spherical lens over the sample at a ≈30° angle with respect to the normal to the film surface, then, forming an ellipse (minor axis of ≈1.1 mm). The emitted light was collected perpendicularly to the device with an optical fiber coupled to the same spectrophotometer used for ASE characterization. The beam divergence was determined from direct measurements of the far-field pattern in a direction perpendicular to the resonator grating lines.

Low-Temperature Spectroscopy in Solution: Low-temperature absorption and emission measurements were carried out in methyl THF of spectroscopic degree purchased from Sigma-Aldrich as the solvent in ≈10^{-4} M of sample concentration in a cryostat OPTISTAT cell from Oxford instruments incorporated on a Varian Cary 5000 UV–Vis–NIR spectrophotometer.

Raman Spectroscopy: Raman spectra were measured in the solid-state at room temperature by using a Bruker Senterra Raman microscope by averaging spectra for 50 min with a resolution of 3–5 cm^{-1}. Three Raman excitations wavelengths at 532, 633, and 785 nm were used. The Raman spectra were collected by using the 1 × 1 camera of a CCD camera operating at −50 °C.

TA Spectroscopy: Ultrafast non-degenerate pump-probe characterization was performed using a Ti:Sapphire laser (800 nm, 1 kHz, 2 mJ). The wavelength of the pump beam was tuned with an optical parametric amplifier (OPA) to match the absorption bands of the NGs. In the case of TT-Ar, the broadband probe beam was generated by directly focusing the 800 nm-beam into a CaF$_2$ plate. On the other hand, the probe beam for PP-Ar was generated by, first, converting the 800 nm-beam into an 1130 nm-beam with an OPA; then, the beam was focused over a YAG plate. The pump and probe beams were overlapped on the same spot of the sample, while keeping a low fluence to avoid damaging it.

2105073 (9 of 10)

[1] A. J. C. Kuehne, M. C. Gather, *Chem. Rev.* **2016**, *116*, 12823.

[2] C. Grivas, *Prog. Quantum Electron.* **2016**, *45*, 3.

[3] Y. Jiang, Y. Y. Liu, X. Liu, H. Lin, K. Gao, W. Y. Lai, W. Huang, *Chem. Soc. Rev.* **2020**, *49*, 5885.

[4] J. J. Wu, X. D. Wang, L. S. Liao, *ACS Photonics* **2019**, *6*, 2590.

[5] G. Hong, A. L. Antaris, H. Dai, *Nat. Biomed. Eng.* **2017**, *1*, 0010.

[6] G. Qian, Z. Y. Wang, *Chem. - Asian J.* **2010**, *5*, 1006.

[7] D. G. Lidzey, D. D. C. Bradley, M. S. Skolnick, T. Virgili, S. Walker, D. M. Whittaker, *Nature* **1998**, *395*, 53.

[8] S. R. Forrest, *Nature* **2004**, *428*, 911.

[9] L. Chen, Y. Hernandez, X. Feng, K. Müllen, *Angew. Chem., Int. Ed.* **2012**, *51*, 7640.

[10] J. V. Caspar, E. M. Kober, B. P. Sullivan, T. J. Meyer, *J. Am. Chem. Soc.* **1982**, *104*, 630.

[11] S. H. Lis, *J. Chem. Phys.* **1970**, *53*, 3766.

[12] J. Clark, G. Lanzani, *Nat. Photonics* **2010**, *4*, 438.

[13] G. M. Paternò, L. Moretti, A. J. Barker, Q. Chen, K. Müllen, A. Narita, G. Cerullo, F. Scotognella, G. Lanzani, *Adv. Funct. Mater.* **2018**, *29*, 1805249.

[14] F. Bonaccorso, Z. Sun, T. Hasan, A. C. Ferrari, *Nat. Photonics* **2010**, *4*, 611.

[15] W. Han, R. K. Kawakami, M. Gmitra, J. Fabian, *Nat. Nanotechnol.* **2014**, *9*, 794.

[16] K. P. Loh, Q. Bao, G. Eda, M. Chhowalla, *Nat. Chem.* **2010**, *2*, 1015.

[17] T. Ohta, A. Bostwick, T. Seyller, K. Horn, E. Rotenberg, *Science* **2006**, *313*, 951.

[18] Q. Chen, C. Zhang, F. Xue, Y. Zhou, W. Li, Y. Wang, W. Tu, Z. Zou, X. Wang, M. Xiao, *Sci. Rep.* **2013**, *3*, 2315.

[19] P. Das, R. Maiti, P. K. Barman, S. K. Ray, B. B. N. Shivakiran, *Nanotechnology* **2016**, *27*, 055201.

[20] D. Yadav, G. Tamamushi, T. Watanabe, J. Mitsushio, Y. Tobah, K. Sugawara, A. A. Dubinov, A. Satou, M. Ryzhii, V. Ryzhii, T. Otsuji, *Nanophotonics* **2018**, *7*, 741.

[21] G. M. Paternò, Q. Chen, X. Y. Wang, J. Liu, S. G. Motti, A. Petrozza, X. Feng, G. Lanzani, K. Müllen, A. Narita, F. Scotognella, *Angew. Chem., Int. Ed.* **2017**, *56*, 6753.

[22] V. Bonal, R. Muñoz-Mármol, F. Gordillo Gámez, M. Morales-Vidal, J. M. Villalvilla, P. G. Boj, J. A. Quintana, Y. Gu, J. Wu, J. Casado, M. A. Díaz-García, *Nat. Commun.* **2019**, *10*, 3327.

[23] K. A. Ritter, J. W. Lyding, *Nat. Mater.* **2009**, *8*, 235.

[24] Y. Gu, R. Muñoz-Mármol, S. Wu, Y. Han, Y. Ni, M. A. Díaz-García, J. Casado, J. Wu, *Angew. Chem., Int. Ed.* **2020**, *59*, 8113.

[25] G. M. Paternò, L. Nicoli, Q. Chen, K. Müllen, A. Narita, G. Lanzani, F. Scotognella, *J. Phys. Chem. C* **2018**, *122*, 25007.

[26] R. Muñoz-Mármol, V. Bonal, G. M. Paternò, A. M. Ross, P. G. Boj, J. M. Villalvilla, J. A. Quintana, F. Scotognella, C. D'Andrea, S. Sardar, G. Lanzani, Y. Gu, J. Wu, M. A. Díaz-García, *Nanomaterials* **2020**, *10*, 1525.

[27] E. M. Calzado, M. G. Ramírez, P. G. Boj, M. A. D. García, *Appl. Opt.* **2012**, *51*, 3287.

[28] M. Anni, A. Perulli, G. Monti, *J. Appl. Phys.* **2012**, *111*, 093109.

[29] T. Cao, F. Zhao, S. G. Louie, *Phys. Rev. Lett.* **2017**, *119*, 076401.

[30] S. Milanese, M. L. De Giorgi, M. Anni, *Molecules* **2020**, *25*, 2992.

[31] Y. Gu, Y. Gopalakrishna Tullimilli, J. Feng, H. Phan, W. Zeng, J. Wu, *Chem. Commun.* **2019**, *55*, 5567.

[32] Ö. H. Omar, D. Padula, D. Troisi, *ChemPhotoChem* **2020**, *4*, 5223.

[33] G. Salvitti, F. Negri, Á. J. Pérez-Jiménez, E. San-Fabián, D. Casanova, J. C. Sancho-García, *J. Phys. Chem. A* **2020**, *124*, 3590.

[34] J. A. Quintana, J. M. Villalvilla, M. Morales-Vidal, P. G. Boj, X. Zhu, N. Ruangsupapichat, H. Tsuji, E. Nakamura, M. A. Díaz-García, *Adv. Opt. Mater.* **2017**, *5*, 1700238.

[35] H. Kogelnik, C. V. Shank, *J. Appl. Phys.* **1972**, *43*, 2327.

[36] R. Kazarinov, C. Henry, *IEEE J. Quantum Electron.* **1985**, *21*, 144.

[37] M. G. Ramírez, M. Morales-Vidal, V. Navarro-Fuster, P. G. Boj, J. A. Quintana, J. M. Villalvilla, A. Retolaza, S. Merino, M. A. Díaz-García, *J. Mater. Chem. C* **2013**, *1*, 1182.

[38] M. Morales-Vidal, P. G. Boj, J. M. Villalvilla, J. A. Quintana, Q. Yan, N.-T. Lin, X. Zhu, N. Ruangsupapichat, J. Casado, H. Tsuji, E. Nakamura, M. A. Díaz-García, *Nat. Commun.* **2015**, *6*, 8458.

[39] V. Bonal, J. A. Quintana, R. Muñoz-Mármol, J. M. Villalvilla, P. G. Boj, M. A. Díaz-García, *Thin Solid Films* **2019**, *692*, 137580.

[40] V. Bonal, J. M. Villalvilla, J. A. Quintana, P. G. Boj, N. Lin, S. Watanabe, K. Kazlauskas, O. Adomeniene, S. Jursenas, H. Tsuji, E. Nakamura, M. A. Díaz-García, *Adv. Opt. Mater.* **2020**, *8*, 2001153.

[41] V. Bonal, J. A. Quintana, J. M. Villalvilla, P. G. Boj, M. A. Díaz-García, *Sci. Rep.* **2019**, *9*, 11159.

[42] S. Grimme, A. Hansen, *Angew. Chem., Int. Ed.* **2015**, *54*, 12308.

[43] C. Angeli, R. Cimiraglia, S. Evangelisti, T. Leininger, J. P. Malrieu, *J. Chem. Phys.* **2001**, *114*, 10252.

[44] S. Grimme, J. G. Brandenburg, C. Bannwarth, A. Hansen, *J. Chem. Phys.* **2015**, *143*, 054107.

[45] F. Neese, *Wiley Interdiscip. Rev.: Comput. Mol. Sci.* **2018**, *8*, 1327.